Gold stabilized by nanostructured ceria supports : nature of the active sites and catalytic performance

Top Catal (2011) 54:424–438
DOI 10.1007/s11244-011-9673-2

ORIGINAL PAPER

Gold Stabilized by Nanostructured Ceria Supports: Nature of the Active Sites and Catalytic Performance

Yejun Guan · D. A. J. Michel Ligthart · Özlem Pirgon-Galin · Johannis A. Z. Pieterse · Rutger A. van Santen · Emiel J. M. Hensen

Published online: 8 February 2011

Abstract The interaction of gold atoms with CeO_2 nanocrystals having rod and cube shapes has been examined by cyanide leaching, TEM, TPR, CO IR and X-ray absorption spectroscopy. After deposition–precipitation and calcination of gold, these surfaces contain gold nanoparticles in the range 2–6 nm. For the ceria nanorods, a substantial amount of gold is present as cations that replace Ce ions in the surface as follows from their first and second coordination shells of oxygen and cerium by EXAFS analysis. These cations are stable against cyanide leaching in contrast to gold nanoparticles. Upon reduction the isolated Au atoms form finely dispersed metal clusters with a high activity in CO oxidation, the WGS reaction and 1,3-butadiene hydrogenation. By analogy with the very low activity of reduced gold nanoparticles on ceria nanocubes exposing the {100} surface plane, it is inferred that the gold nanoparticles on the ceria nanorod surface also have a low activity in such reactions. Although the finely dispersed Au clusters are thermally stable up to quite high temperature in line with earlier findings (Y. Guan and E. J. M. Hensen, Phys Chem Chem Phys 11:9578, 2009), the presence of gold nanoparticles results in their more facile agglomeration, especially in the presence of water (e.g., WGS conditions). For liquid phase alcohol oxidation, metallic gold nanoparticles are the active sites. In the absence of a base, the O–H bond cleavage appears to be rate limiting, while this shifts to C–H bond activation after addition of NaOH. In the latter case, the gold nanoparticles on the surface of ceria nanocubes are much more active than those on the surface of nanorod ceria.

Keywords Gold · Ceria · Particle size · Active sites · Reduction · Oxidation

Y. Guan · D. A. J. M. Ligthart · R. A. van Santen · E. J. M. Hensen (✉)
Schuit Institute of Catalysis, Eindhoven University of Technology, P.O. Box 513, 5600 MB Eindhoven, The Netherlands
e-mail: e.j.m.hensen@tue.nl

Ö. Pirgon-Galin · J. A. Z. Pieterse
Energie Centrum Nederland, P.O. Box 1, 1755 ZG Petten, The Netherlands

1 Introduction

Gold nanoparticles stabilized by reducible transition metal oxides can efficiently catalyze many interesting reactions [1–3], the most notable one being the low temperature oxidation of CO as first described by Haruta et al. [4]. Of determining importance appear to be the size of the metal nanoparticles or clusters, the ability of the support to provide oxygen atoms during catalytic reactions and the influence of the oxidation state of the gold atoms in close proximity to the surface. Among the reducible oxides, ceria (CeO_2) is one of the most efficient supports, because of its capability to store oxygen and become reduced [5, 6]. Ceria-supported gold has been shown to catalyze important reactions such as CO oxidation [7, 8], alcohol oxidation [9], hydrogenation [10, 11] and the water–gas shift (WGS) reaction [12].

The active site in Au/CeO_2 catalysts will not be the same for all these reactions. Au^{3+}, Au^{+} and Au^{0} are known to exist in different proportions in ceria-supported Au catalysts. The exact surface composition will depend on the method of preparation and pretreatment and the metal loading. For instance, Gates and co-workers considered that there is a strong possibility that there are multiple reaction channels for catalysis of CO oxidation by supported gold, involving gold in different oxidation states [3]. For the WGS reaction, isolated gold cations have been

claimed as the active sites [12], although more recently there appears to be consensus that metallic gold cluster are the active sites [13, 14]. A similar debate is apparent about the active sites in alkene hydrogenation [11, 15–17].

In line with the importance of the interactions between gold and the support, it has been found that nanoscale forms of ceria contribute to the high activity of small gold particles [18–24]. Several authors [25–28] have used nanostructured ceria that expose certain planes to investigate the influence of the nature of the ceria surface on the nature and activity of gold species. By judicious choice of the hydrothermal treatment conditions of hydrolyzed cerium(III) salts, single-crystalline nanopolyhedra, nanorods and nanocubes were obtained [29, 30]. The results of such studies confirm the strong effect of the crystal plane of ceria on the activity of gold for the WGS and CO oxidation reactions. Gold particles on {110} planes as present on nanorods are more active than those stabilized by {100} planes of nanocubes.

The surface of ceria has been very extensively studied by experimental and theoretical methods. In relation to gold catalysis, it has been argued that surface defects like cerium and oxygen vacancies play a role in the nucleation and stabilization of gold nanoparticles [31–36]. Another relevant issue is the stabilization of cationic gold in ceria, either at the surface or as a solid solution. Several authors have discussed the substitution of Ce^{3+}/Ce^{4+} by Au^{3+} [20, 37–40]. Recently, EXAFS structure analysis showed that the isolated Au cations in leached Au/CeO_2 are surrounded by oxygen and cerium, respectively, in the first and second coordination shell in agreement with Au substitution for Ce [11]. Thermodynamically, the adsorption of Au on O vacancies is favored over adsorption on Ce vacancies [33, 40].

In this work, we use the approach of ceria exposing certain crystal planes (nanorods and nanocubes) to stabilize gold nanoparticles to investigate in detail the nature of the gold phase before and after leaching with cyanide. In situ X-ray absorption spectroscopy, transmission electron microscopy, temperature programmed reduction and CO IR spectroscopy are used to study the surface of the Au/CeO_2 catalysts. By comparing the activity of these catalysts in a wide range of reactions (CO oxidation, alcohol oxidation, butadiene hydrogenation, WGS), we aim to provide further insight into the active site requirements for the various types of reactions.

2 Experimental

2.1 Synthesis of Materials

2.1.1 Nanostructured CeO_2

CeO_2 support materials with controlled crystal shapes were prepared according to literature procedures [30, 41]. Typically, 40 mL of 0.5 M $Ce(NO_3)_3$ aqueous solution and 60 mL of 10 M NaOH solution were added to a 125 mL Teflon-lined stainless-steel autoclave and stirred for 30 min at room temperature. The sealed autoclave was then transferred to an oven at 373 K (nanorods) or 453 K (nanocubes) and kept at this temperature for 24 h. Subsequently, the precipitate was filtered and thoroughly washed by distilled water several times until the pH of the filtrate was 7. Finally, the precipitate was dried at 383 K overnight and calcined at 773 K in air for 4 h. The rod- and cube-shaped crystals are denoted by CeO_2(rod) and CeO_2(cube), respectively. The powder X-ray diffraction (XRD, Bruker D4, Cu Kα) show the cubic fluorite structure of CeO_2 (space group: *Fm3m*) for these two materials.

2.1.2 Au/CeO_2 Catalysts

Gold catalysts were prepared by deposition–precipitation of gold on the ceria supports [11, 12]. In a typical synthesis, the desired amount of $HAuCl_4$ and urea were dissolved in 100 mL of distilled water. After addition of 2 g of ceria, the solution was refluxed at 363 K for 2 h. Subsequently, the solid was filtered, dried at 383 K and optionally calcined at 673 K. The target gold loadings were 1, 2 and 6 wt%. A portion of the catalysts was treated with a cyanide-containing solution. An amount of the catalyst was suspended in a 2 wt% NaCN solution (CN/Au molar ratio = 2) at a pH of 12 by addition of NaOH and stirred overnight under aeration. After this leaching treatment, the resulting suspension was filtered, dried at 383 K overnight and calcined at 673 K for 4 h in air. The gold catalysts are denoted by Au/CeO_2(crystal shape)-CN with the optional postfix to indicate the leaching treatment.

2.2 Characterization of Materials

2.2.1 Elemental Analysis

The gold loading was determined by inductively coupled plasma atomic emission spectroscopy (ICP-OES) analyses performed on a Goffin Meyvis SpectroCirus^{ccd} apparatus. The samples were dissolved in a 3:1 HCl/HNO_3 solution.

2.2.2 XRD

Powder XRD diffractograms were recorded on Bruker D4 Endeavour (Cu Kα, scan between 10 and 80°, 0.02° per step and 2.5 s per step).

2.2.3 Textural Properties

The BET surface area was measured by nitrogen adsorption at 77 K on a Micromeretics Tristar 3000 analyzer after drying the materials at 423 K.

2.2.4 Transmission Electron Microscopy

Electron micrographs of the support materials and catalysts were taken with a FEI Tecnai 20 electron microscope at an acceleration voltage of 200 kV with a LaB_6 filament. Typically, a small amount of sample was ground and suspended in ethanol, sonicated and dispersed over a Cu grid with carbon film.

2.2.5 Temperature-Programmed Reduction (TPR)

TPR experiments were carried out in a flow apparatus equipped with a fixed-bed reactor, a computer-controlled oven and a thermal conductivity detector. Typically, an amount of catalyst was contained between two quartz wool plugs in a quartz reactor. Prior to TPR, the catalyst was oxidized by exposure to a flowing mixture of 4 vol% O_2 in He under heating to 723 K at a rate of 10 K/min. After the sample was cooled to room temperature in flowing nitrogen, the sample was reduced in 4 vol% H_2 in N_2 at a flow rate of 8 mL/min, whilst heating from room temperature up to 1073 K at a ramp rate of 10 K/min. The H_2 signal was calibrated using a CuO/SiO_2 reference catalyst.

2.2.6 Infrared Spectroscopy of Adsorbed CO

Infrared spectra were recorded at room temperature on a Bruker IFS-113v Fourier transform IR spectrometer with a DTGS detector at a resolution of 4 cm^{-1}. Typically, a wafer was prepared with a density of $\sim$10 mg/cm^2 and placed in a controlled atmosphere cell. The sample was pretreated in oxygen or hydrogen at the desired temperature for 1 h. Subsequently, the cell was evacuated to a pressure lower than 10^{-6} mbar and the sample was cooled to 80 K. An initial infrared spectrum was recorded that served as the background for further spectra. Small doses of CO ($\sim$0.4 μmol) were introduced into the cell followed by recording an IR spectrum until saturation of the bands in the carbonyl stretching region. FTIR spectra of adsorbed CO were then recorded intermittent to the following treatment scheme: (i) reduction by H_2 at 393 K, (ii) reoxidation at 313 K, (iii) reduction at 773 K and (iv) reoxidation at 313 K. Each step was followed by extensive evacuation and cooling to 80 K.

2.2.7 X-Ray Absorption Spectroscopy (XAS)

X-ray absorption measurements were carried out at the Dutch-Belgian Beamline (Dubble) at the ESRF (France). Data were collected at the Au L_{III} edge in fluorescence mode with a 9-channel solid-state detector. To decrease the strong fluorescent radiation caused by cerium, an aluminum foil (thickness 60 μm) was placed in front of the fluorescence detector. Energy selection was done by a double crystal Si(111) monochromator. Background removal was carried out by standard procedures with the Viper software. EXAFS analysis was then performed with EXCURVE931 on k^3-weighted unfiltered raw data using the curved wave theory. Phase shifts were derived from ab initio calculations using Hedin–Lundqvist exchange potentials and Von Barth ground states. Energy calibration was carried out with a gold foil. The amplitude reduction factor S_0^2 associated with central atom shake-up and shake-off effects was set at 0.88 by calibration of the first- and second-shell Au–Au coordination numbers to 12 and 4, respectively, for k^3-weighted EXAFS fits of the Au foil. The whiteline of the XANES part of the absorption spectrum was fitted by linear combinations of reference catalysts by a least-squares method.

Spectra at the Au L_{III} edge were recorded in a stainless-steel controlled atmosphere cell. The cell was heated with two firerods controlled by a temperature controller via a thermocouple placed close to the catalyst sample. Typically, an amount of 100 mg of sample was pressed in a stainless steel holder and placed in the cell. High-purity carbon foils with a thickness of 150 μm were used as windows. High-purity gases (He, 5 vol% H_2 in He or 20 vol% O_2 in He) were delivered by Bronkhorst thermal mass flow controllers. The total gas flow was kept at 20 mL/min. The catalyst sample was heated in He to 393 K at a rate of 10 K/min. EXAFS spectra were recorded after cooling to room temperature. For the high-loading catalyst three consecutive scans were measured, while for the low-loading catalysts six scans were averaged. For in situ WGS experiments the feed consisted of a flow of 5.8 vol% CO and 11.6 vol% H_2O in He at a total flow rate of 50 mL/min. The CO conversion was determined by a Agilent MicroGC system equipped with a Porapak Q column with a thermal conductivity detector.

2.3 Catalytic Activity Measurements

The catalytic activity in the oxidation of carbon monoxide and the hydrogenation of 1,3-butadiene was evaluated in a parallel ten-flow microreactor system. The effluent products (CO, CO_2 and O_2 for CO oxidation and 1,3-butadiene, butenes and butanes for 1,3-butadiene hydrogenation) were analyzed by an Interscience CompactGC online gas chromatograph equipped with Porapak Q (TCD), Molecular sieve 5A (TCD) and a PLOT KCl/Al_2O_3 columns (FID). For CO oxidation, the feed mixture contained 1 vol% CO and 1 vol% O_2 in He at a total flowrate of 100 mL/min. An amount of 15 mg of catalyst was diluted with 250 mg of SiC of the same sieve fraction and contained between two quartz wool plugs in a quartz reactor with an internal diameter of 4 nm. CO conversion was determined in the

temperature range from 293 to 373 K. Hydrogenation of 1,3-butadiene was carried out at 383 K in a mixture of 2 vol% 1,3-butadiene in H_2 at a total flow rate of 20 mL/min. Prior to reaction, the catalysts were pretreated at 393 K in a flow of 10 vol% H_2 in He.

The water gas shift (WGS) reaction was carried out in a quartz reactor with an internal diameter of 4 mm. Typically, an amount of 50 mg catalyst was used. The feed flow was 40 mL/min and consisted of 40 vol% N_2, 20 vol% H_2O, 20 vol% H_2, 10 vol% CO and 10 vol% CO_2. Prior to reaction, the catalyst was reduced in a mixture of 5 vol% H_2 in N_2 under heating from 293 to 453 K at a rate of 2 K/min.

The aerobic oxidation of benzyl alcohol was carried out as previously reported [42]. A round-bottle flask (25 mL) was charged with 100 mg of catalyst, 1 mmol of benzyl alcohol and 9.9 mL of toluene. Some experiments were carried out in the presence of 40 mg NaOH. In such case, the catalyst amount was kept at 50 mg to avoid complete conversion under otherwise similar conditions. Molecular oxygen was bubbled through the reaction mixture at a flow rate of 20 mL/min. The resulting mixture was then heated at 373 K for 1 h and cooled to room temperature. The reaction products were analyzed by a Shimadzu QP 5050 GC-MS (CP-Sil 8CB, 50 m × 0.32 mm, $d_f = 0.15$ μm).

3 Results and Discussion

Figure 1 shows representative transmission electron micrographs of CeO_2 nanorods and nanocubes. The ceria rods have a typical width of 6.5 ± 1.6 nm with a broad length distribution between 30 and 200 nm. The ceria nanocubes have a size distribution ranging from 20 to 60 nm. The exposed surfaces for CeO_2 nanorods have mostly been confirmed as {110} and {100} planes [26, 30, 41]. Although the *d*-spacing along the long side of CeO_2(rod) of 0.31 nm by analysis of our TEM images suggests the presence of {111} planes in line with recent other work [43], we adopt here the assignment of {110} planes. A more detailed EM analysis would be necessary to resolve this issue for our ceria nanorods. The surface of CeO_2(rod) exhibits a defective structure, which is thought to be due to the presence of oxygen vacancies in the

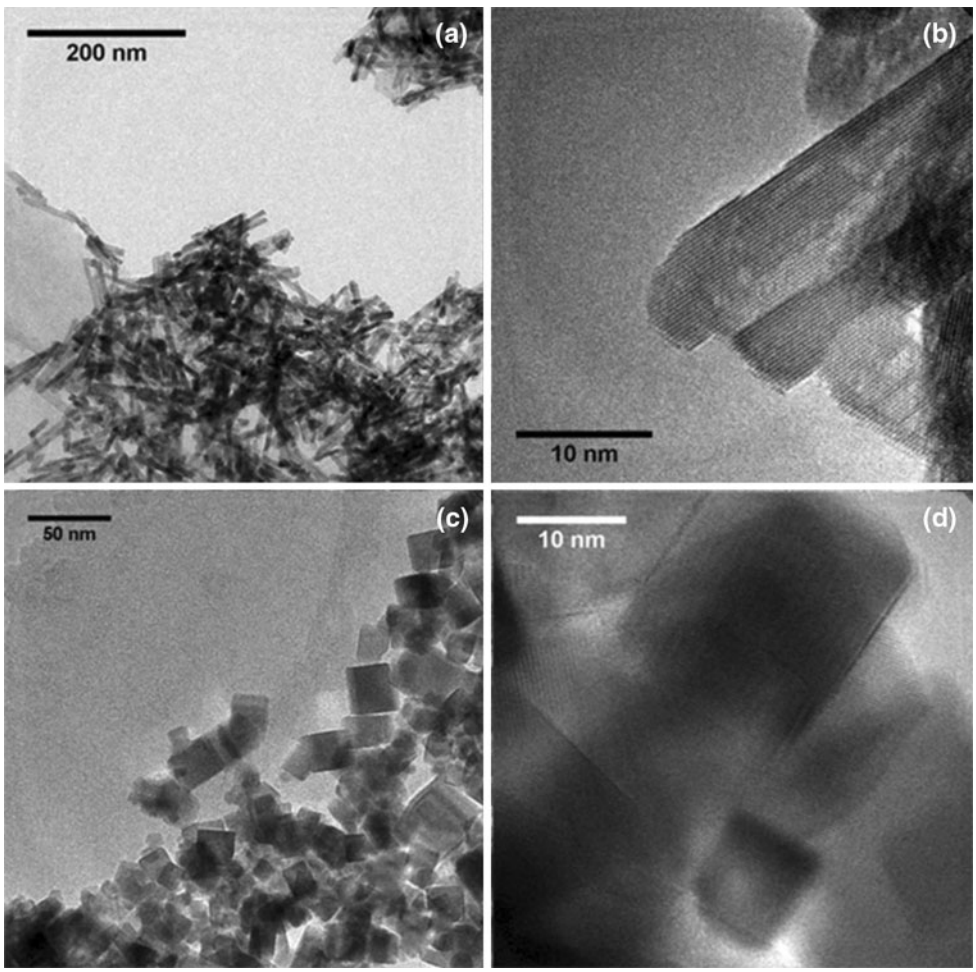

Fig. 1 Transmission electron micrographs of **a**, **b** CeO_2(rod) and **c**, **d** CeO_2(cube)

surface. The {100} plane with a *d*-spacing of 0.27 nm dominates on CeO_2(cube) [30]. The crystallite sizes determined by application of Scherrer's equation are 8 and 35 nm for CeO_2(rod) and CeO_2(cube), respectively. The reason for the lower crystallite size of the CeO_2(rod) is the lower synthesis temperature compared to the due to their synthesis at lower temperature than employed for CeO_2 (cube). This difference is consistent with the BET surface areas of 24 m^2/g for CeO_2(cube) and 110 m^2/g for CeO_2(rod).

Figure 2 displays representative transmission electron micrographs of gold nanoparticles supported by CeO_2(rod) and CeO_2(cube) at a metal loading of 2 wt%. The size of the gold particles is in the range of 2–8 nm. The average particle size is 4.6 ± 1.5 and 4.7 ± 1.5 nm for Au/CeO_2(rod) and Au/CeO_2(cube), respectively. The values are close to the particle size of 4.0 nm determined for a 2 wt% Au supported on polyhedral ceria [11]. Most gold nanoparticles have a pyramidal shape. This has led others to propose that the atoms in the top layers of such particles are metallic, while those atoms that form the interface with the support are oxidic [44–46].

Upon cyanide leaching of these materials, the gold loading has decreased substantially (Table 1). The leached Au/CeO_2(rod) catalyst contains 0.38 wt% Au. The gold loading in Au/CeO_2(cube)-CN is lower than the detection limit of 0.01 wt%. These results are in qualitative agreement with those obtained by Si and Flytzani-Stephanopoulos [26]. The electron micrographs of both leached catalysts do not show gold nanoparticles anymore, indicating that leaching is effective in removing the large nanoparticles in the parent materials. These results are in agreement with our earlier reported results [11].

In order to obtain more insight into nature of the interaction of gold with the ceria surfaces, the leaching procedure was carried out for a set of ceria nanorod- and nanocube-supported catalysts with varying gold loading. Table 1 shows that the amount of gold retained by CeO_2(rod) upon leaching does not strongly depend on the gold loading of the parent material. For a set of Au/CeO_2(cube) gold was completely removed by cyanide leaching. To establish at what stage of the preparation the specific interaction of gold with the ceria surface is brought about, cyanide leaching was carried out on a Au/CeO_2(rod)

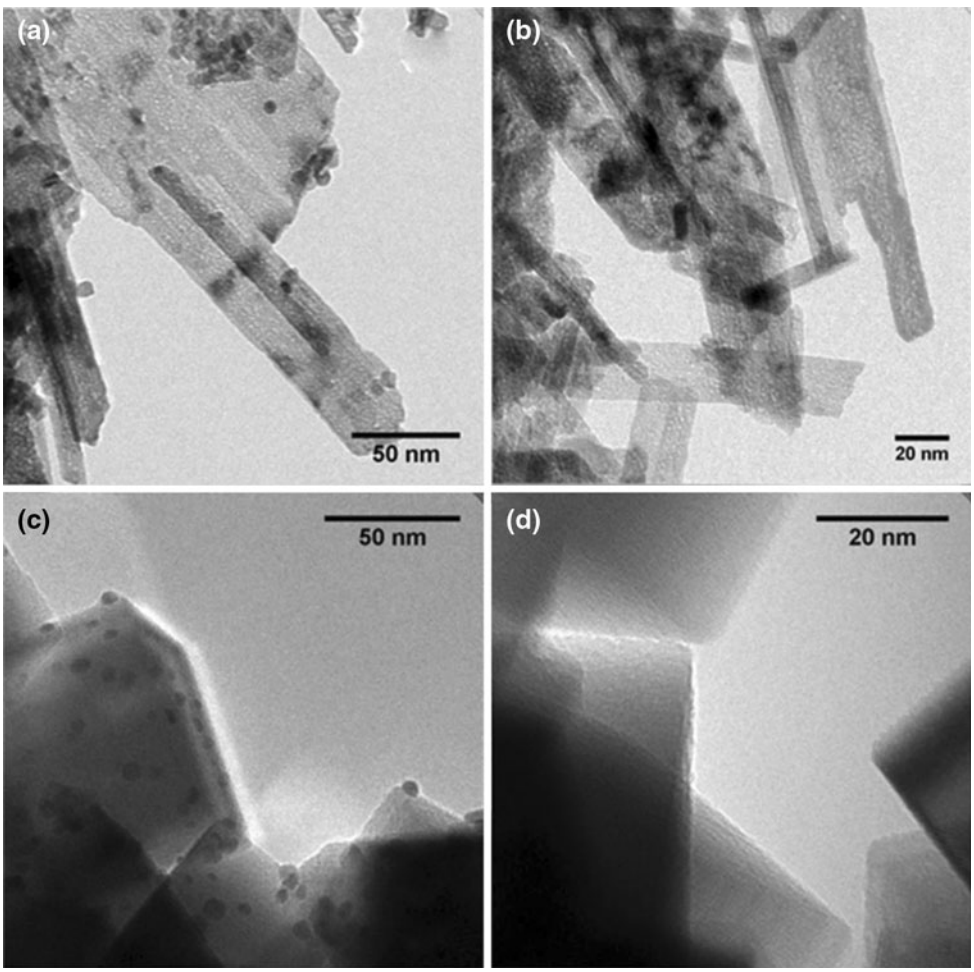

Fig. 2 Transmission electron micrographs of **a** Au/CeO_2(rod), **b** Au/CeO_2(rod)-CN, **c** Au/CeO_2(cube) and **d** Au/CeO_2(cube)-CN

Table 1 Metal loading of ceria-supported gold catalysts before and after leaching by a NaCN solution

Support	Pretreatment	Au loading (wt%)	
		Before leaching	After leaching
CeO_2(rod)	Calcination	0.79	0.29
		2.01	0.38
		3.30	0.35
		6.02	0.22
	Drying	2.01	0.08
CeO_2(cube)	Calcination	1.90	<0.01
		4.29	<0.01

catalyst that had not been calcined after deposition–precipitation. Instead, the precursor has been dried at 333 K. In this case, the gold loading after leaching was only 0.086 wt% indicating that the strong metal-support interaction is brought about by calcination of the catalyst precursor. In this material gold is predominantly present as gold hydroxides. The function of the cyanide ions is then to complex the gold cations. A final experiment was done to exclude the possibility that the strong interaction between gold and the surface of CeO_2(rod) is brought about during the leaching process. To this end, cyanide leaching of Au/CeO_2(rod) was carried out followed by filtration. The filtrate was brought in contact with fresh CeO_2(rod) and was then filtered again. The gold loading of this material was 0.089 wt%. The finding that the amount of gold adsorbed in this case is close to the amount remaining after leaching of the non-calcined catalyst may indicate that part of the gold on CeO_2 is adsorbed at vacancies in the ceria surface during such treatments.

Hydrogen TPR measurements were carried out to determine differences in the reducibility of the catalysts. Figure 3 contains the TPR traces for the catalysts and Table 2 collects the maxima of the TPR traces and the total hydrogen consumption for the supports and the catalysts. The higher hydrogen uptake of CeO_2(rod) (571 μmol/g) than that of CeO_2(cube) (121 μmol/g) is due to the difference in surface area. The reduction of the support materials (not shown) takes place in the region 723–823 K in agreement with results for conventional CeO_2 [47]. The reduction of Au/CeO_2(rod) and Au/CeO_2(rod)-CN occurs around 430 K. The hydrogen uptake takes place in a much broader temperature range for the former catalyst than for the latter. The hydrogen uptake of Au/CeO_2(rod) is slightly higher than that of the support, whereas the uptake of Au/CeO_2(rod)-CN is close to the value determined for the support. This result confirms that nearly all surface oxygen species of ceria can be reduced at low temperature, even in the presence of a relatively small amount of gold as in Au/CeO_2(rod)-CN [18, 48]. The somewhat higher uptake of

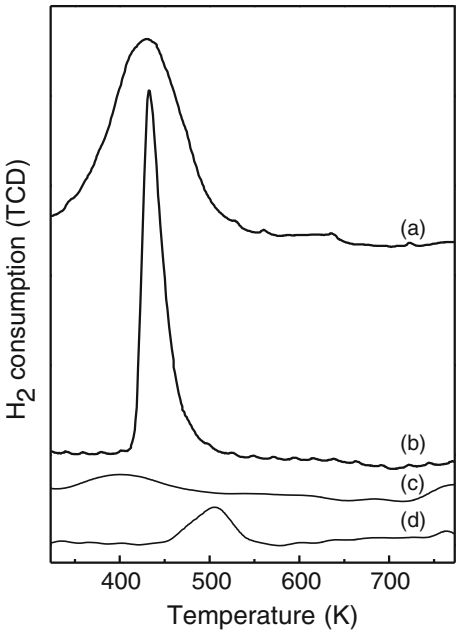

Fig. 3 TPR traces of hydrogen consumption (positive means consumption) for *a* Au/CeO_2(rod), *b* Au/CeO_2(rod)-CN, *c* Au/CeO_2(cube) and *d* Au/CeO_2(cube)-CN

Table 2 Maximum of hydrogen reduction peak and total hydrogen uptake during TPR of supports and catalysts

Sample	T_{max} (K)	Hydrogen uptake (μmol/g)
CeO_2(rod)	773	570
CeO_2(cube)	773	121
Au/CeO_2(rod)	429	670
Au/CeO_2(rod)-CN	433	541
Au/CeO_2(cube)	403	44
Au/CeO_2(cube)-CN	513	45

Au/CeO_2(rod) is probably due to the reduction of gold surface oxides. Typically, calcination of the gold hydroxide precursor phase results in gold metal nanoparticles with some residual surface oxygen [49]. As a large fraction of gold is already reduced, hydrogen atoms from H_2 dissociation by gold spill over to the ceria support and reduce its surface [50–52]. The hydrogen uptake for the cyanide-leached Au/CeO_2(rod) takes place in a much smaller temperature range. This indicates that the gold particles are oxidic and that they are more difficult to reduce than the gold nanoparticles in the parent material. The reduction in Au/CeO_2(cube) takes place at relatively low temperature. Interestingly, the hydrogen uptake is substantially lower than that of the parent ceria nanocube support. After cyanide leaching, a hydrogen uptake feature is observed around 525 K. It might be that this latter feature is due to the partial surface reduction of CeO_2(cube) facilited by the

reduction of the residual gold cations in this surface to metallic particles. The total uptake of Au/CeO_2(cube)-CN is similar to that of Au/CeO_2(cube). It should be noted that the TPR traces of the nanocube-supported catalysts show a slight increase of the hydrogen consumption at the high temperature end. This may indicate that hydrogen spillover processes are less efficient on the cube-shaped ceria surface planes than they are on the rod-shaped planes and complete surface reduction only occurs at high temperatures.

Figure 4 compares FTIR spectra after CO adsorption at 80 K for the various gold catalysts. The spectrum in the carbonyl region for the fresh Au/CeO_2(rod) catalysts exhibits a broad band centered around 2130 cm^{-1} with shoulders at 2116 and 2207 cm^{-1}. The band at 2130 cm^{-1} may be assigned to CO adsorbed to positively charged gold species [19, 53], but care has to be taken because this band overlaps with the band due to CO adsorption to Ce^{3+} centers [54, 55]. The band at 2116 cm^{-1} is due to the adsorption of CO to metallic gold [56]. Boccuzzi et al. [57–59] have proposed that CO stretching band on gold nanoparticles in the range of 2106–2118 cm^{-1} relates to CO adsorption to corner sites. The band at 2207 cm^{-1} is likely due to CO adsorbed to Au^{3+} [55]. Figure 4 shows the corresponding IR spectrum of the calcined Au/CeO_2(cube) catalyst. A strong band at 2117 cm^{-1} is observed, indicative of the presence of neutral gold nanoparticles [56]. The bands around 2130 and 2207 cm^{-1} present in the spectra of Au/CeO_2(rod) are not observed, which suggests that this sample does not contain cationic gold species. The absence of the band at 2130 cm^{-1} also shows that the surface of ceria nanocubes does not contain Ce^{3+} vacancies. These FTIR spectra considerably changed following reduction in H_2 at 393 K. The band at 2130 cm^{-1} becomes much more intense (Fig. 4), which should be due to the increased density of Ce^{3+} sites at the surface. New bands appear at 2028, 2084, and 2103 cm^{-1}. The former two bands are assigned to CO adsorption on anionic gold clusters [56, 58, 59]. The latter band at 2103 cm^{-1} has been assigned to CO adsorption on well-reduced gold particles. This band replaces the one at 2116 cm^{-1}, which has previously been assigned to CO adsorption on metallic gold in the presence of surface oxygen species [58]. This latter assignment agrees with the changes in the band's position upon reduction.

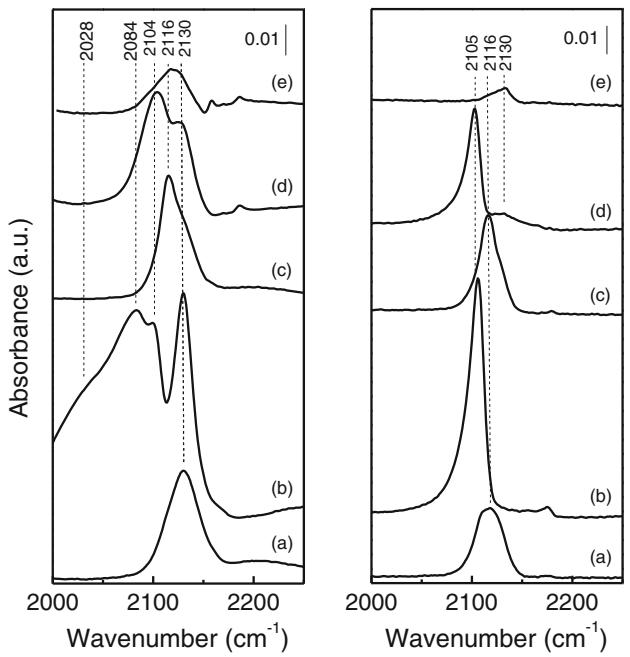

Fig. 4 FTIR spectra of adsorbed CO at 80 K of (*left*) Au/CeO_2(rod) and (*right*) Au/CeO_2(cube): *a* fresh calcined catalyst, *b* reduction at 393 K, *c* reoxidation at 423 K, *d* reduction at 773 K and *e* reoxidation at 313 K

In contrast to these results, the corresponding spectrum (Fig. 4) of Au/CeO_2(cube) does not show an increase of the band at 2130 cm^{-1}. This corresponds to the earlier noted absence of reduction of the surface of CeO_2(cube) at low temperatures. More importantly, the observation of a single band for gold at 2105 cm^{-1} indicates that gold is present as reduced gold nanoparticles. The substantial difference in the IR spectra between Au/CeO_2(cube) and Au/CeO_2(rod) may be due to the presence of very finely dispersed gold clusters in strong interaction with the support in the latter catalyst. These particles are not observed by conventional bright-field TEM. The less likely alternative is that the nanoparticles visible by TEM in both catalysts behave completely different.

Upon exposure of the reduced catalysts to O_2 at 313 K the band at 2116 cm^{-1} appeared again at the expense of the one around 2105 cm^{-1} in Au/CeO_2(rod) and Au/CeO_2 (cube). This effect can be understood by the presence of surface oxygen adatoms and has been reported before for both ceria- and silica-supported gold nanoparticles [58, 60]. Another observation is the disappearance of the bands below 2100 cm^{-1}. This could be due to the oxidation of the very fine clusters of gold on the ceria surface in Au/CeO_2(rod). To investigate the stability of the gold nanoparticles against sintering at high temperature, the sample was further reduced at 773 K. In the case of Au/CeO_2(rod) the bands at 2084 and 2103 cm^{-1} were recovered, but with a much lower intensity. This indicates that the gold clusters and particles have substantially sintered. Expectedly, the same shift of the band at 2117 cm^{-1} towards lower wavelength was observed after high-temperature reduction of Au/CeO_2(cube). Also in this case the intensity is much lower, suggesting that the nanoparticles have grown in size.

Figure 5 contains the FTIR spectra for the leached Au/CeO_2 catalysts. The spectrum of Au/CeO_2(rod)-CN after reduction at 393 K contains only a weak feature around 2130 cm^{-1}. After oxidation this band disappears.

Reduction at 523 K results in the appearance of a dominant band around 2130 cm^{-1} due to surface Ce^{3+} states with a shoulder in the region 2105–2115 cm^{-1} due to reduced gold clusters. A weak feature around 2082 cm^{-1} is also observed. Reoxidation at 313 K results in the disappearance of all bands, indicating that the small gold particles were oxidized. Reduction at 773 K results in bands at 2103 and 2130 cm^{-1}. Clearly, these particles are still very small, because reoxidation at 313 K erodes all bands. The corresponding spectra of Au/CeO_2(cube)-CN show no bands for the fresh catalyst and after reduction at 393 K. This agrees with the absence of a TPR feature below 513 K for this catalyst. After reduction at 523 K two prominent bands are observed with a much lower intensity than the other catalysts. The one at 2128 cm^{-1} is due to Ce^{3+} and the one at 2090 cm^{-1} should be due to very finely dispersed gold clusters. Similar to Au/CeO_2(rod)-CN, these bands erode upon reoxidation, even after high temperature reduction. The observation of a CO IR band at 2090 cm^{-1} at this very low Au loading (<0.01 wt%) points to a very high gold dispersion.

X-ray absorption spectroscopy is a useful technique to obtain detailed information about the oxidation state and structure of small supported gold particles [61–65]. Au L_{III} near-edge spectra at room temperature, drying and reduction at various temperatures for Au/CeO_2(rod), Au/CeO_2(rod)-CN and Au/CeO_2(cube) are collected in Fig. 6. The dried Au/CeO_2(rod) catalysts contain a whiteline at

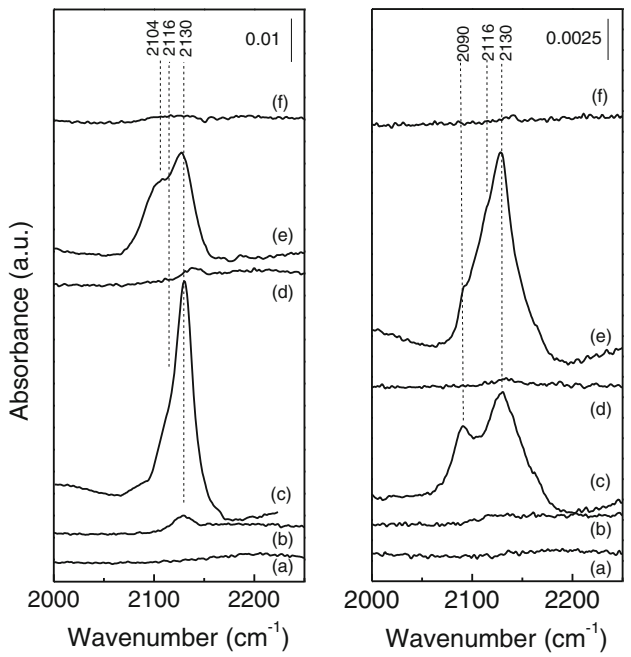

Fig. 5 FTIR spectra of adsorbed CO at 80 K of (*left*) Au/CeO_2(rod)-CN and (*right*) Au/CeO_2(cube)-CN: *a* fresh calcined catalyst, *b* reduction at 393 K, *c* reduction at 423 K, *d* reoxidation at 423 K, *e* reduction at 773 K and *f* reoxidation at 313 K

~4 eV above the edge, which is typical for Au^{3+} compounds [62]. This feature is more intense for the leached catalyst, indicating that a larger fraction of the gold atoms is in the cationic form. The whiteline is nearly absent for Au/CeO_2(cube). Quantification of the amount of cationic gold was carried out by fitting the near-edge spectra by linear combinations of the XANES spectra of a gold foil and that of Au/CeO_2(CN) [11]. The latter catalyst exclusively contained cationic gold as was evident from the EXAFS data analysis. The fraction of cationic gold in these materials as a function of the pretreatment conditions is given in Fig. 7. Au/CeO_2(rod)-CN only contains cationic gold after preparation. Reduction at 393 K in H_2 leads to a substantial decrease of the fraction of cationic gold. After reduction at 473 K only 9% cationic gold is left. To completely reduce the gold a temperature of 773 K is required. The fraction of cationic gold in Au/CeO_2(rod) is initially much lower and then decreases similarly to Au/CeO_2(rod)-CN to very low levels at 773 K. The fresh Au/CeO_2(cube) catalyst contains nearly 90% reduced gold atoms. This amount is nearly independent of the reduction temperature.

Table 3 shows the fit parameters of the Fourier transformed k^3-weighted EXAFS functions for Au/CeO_2(rod), Au/CeO_2(rod)-CN and Au/CeO_2(cube). The FT functions of the EXAFS functions and the fits for the Au/CeO_2(rod) catalysts are shown in Fig. 8. The FT EXAFS spectrum of dried Au/CeO_2(rod) contains a Au–Au shell at a coordination distance (R) of 2.84 Å with a coordination number (CN) of 7.3. It also contains a small contribution of an oxygen backscatterer. These data point to the presence of metallic, yet not fully reduced gold nanoparticles with a particle size of about 3–4 nm [66]. Reduction at 523 K results in the disappearance of the Au–O shell and a small increase of the Au–Au shell. Further reduction at 773 K induces a slightly higher CN and a longer bond distance. The spectrum of dried Au/CeO_2(rod)-CN is completely different and can only be fitted by the inclusion of a Ce backscatterer next to a Au–O shell. The first coordination shell contains ~3 oxygen atoms at $R = 1.99$ Å. The features at larger distance could not be fitted with a Au shell, as present in gold metal or in gold oxide (Au_2O_3: 3.03 and 3.34 Å [67]). This excludes the presence of small gold or gold oxide nanoparticles. Thus, a reasonable fit was obtained by including a Au–Ce shell at $R = 3.27$ Å. The structural parameters point to the presence of gold substituting at a cerium vacancy. These structural features were previously also found for leached Au/CeO_2 [11]. Reduction at 523 K results in a complete change of the structure around the gold atoms. The fit parameters show a Au–Au contribution at $R = 2.74$ Å with CN = 4.0 and a small contribution of oxygen at $R = 1.95$ Å. The Ce shell has disappeared. In agreement with the XANES results, this implies that the gold cations were reduced and have transformed into very

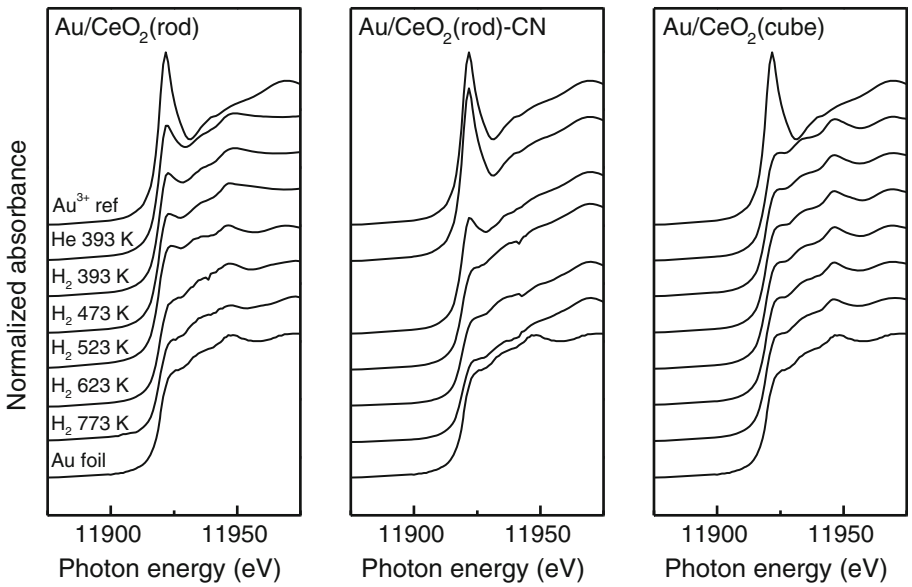

Fig. 6 Near-edge spectra at the Au L_{III} edge of (*left*) Au/CeO_2(rod), (*middle*) Au/CeO_2(rod)-CN and (*right*) Au/CeO_2(cube). *Top* and *bottom* spectra are those of fresh Au/CeO_2(rod)-CN and a Au foil, respectively. The remaining spectra were obtained (from *bottom* to *top*) heating in He at 393 K, reduction at 393 K, reduction at 473 K, reduction at 523 K, reduction at 623 K and reduction at 773 K

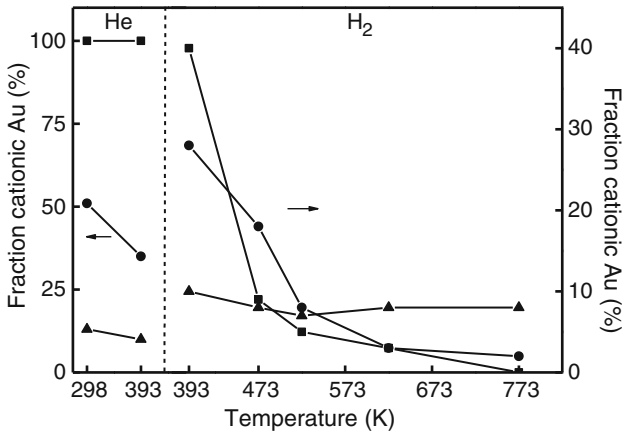

Fig. 7 Fraction of cationic gold after heating in He and H_2 at various temperature as determined by analysis of the near-edge spectra of *filled circle* Au/CeO_2(rod), *filled square* Au/CeO_2(rod)-CN and *filled triangle* Au/CeO_2(cube)

Table 3 Fit parameters of k^3-weighted EXAFS spectra at the Au L_{III} edge of Au/CeO_2 catalysts after different pretreatments

Sample	Treatment	EXAFS fit parameters				
		Shell	R (Å)	CN	$\Delta\sigma^2$ (Å^2)	E_0 (eV)
Au/CeO_2(rod)	He, 393 K	O	1.96	0.7	0.005	−6.2
		Au	2.82	7.3	0.012	
	H_2, 523 K	Au	2.82	7.6	0.010	−7.5
	H_2, 773 K	Au	2.84	8.0	0.011	−7.1
Au/CeO_2(rod)-CN	He, 393 K	O	1.99	3.4	0.007	−8.9
		Ce	3.27	3.8	0.012	
	H_2, 523 K	O	1.95	0.2	0.001	−1.6
		Au	2.74	4.0	0.013	
	H_2, 773 K	O	2.06	0.3	0.006	−5.0
		Au	2.78	7.2	0.015	
Au/CeO_2(cube)	H_2, 523 K	Au	2.86	8.7	0.009	−8.6
	H_2, 773 K	Au	2.86	8.5	0.010	−7.9

Δk = 2.5–10.4 Å^{-1}; estimated error in R ±0.02 Å, N ±20%, $\Delta\sigma^2$ ±10%; normalized residual of fits is between 30 and 36%

small metallic clusters. The relatively short Au–Au distance is in line with the small size of the particles in this catalyst [66, 68–70]. The very low coordination number suggests that the particles have subnanometer dimensions [11, 61]. Upon reduction of the catalyst at 773 K, CN and R for the Au–Au shell increase to 7.2 and 2.78 Å, respectively. These changes point to sintering of the small clusters to larger particles. The decreasing contribution of oxygen neighbours may be attributed to the decreasing interaction with the support or more complete reduction. The EXAFS fit parameters of Au/CeO_2(cube) reduced at 523 K and 773 K evidence the presence of well-reduced gold nanoparticles of around 4 nm.

To obtain more insight into the structure–activity relations of ceria-supported gold catalysts, we have compared the catalytic performance of the nanostructured gold catalysts in a number of commonly used oxidation and hydrogenation reactions (Table 4). The nanostructured ceria supports were not active in CO oxidation at temperatures below 373 K. In line with previous reports [25–27] the turnover frequencies (TOF) follow the trend Au/CeO_2(rod) > Au/CeO_2(rod)-CN > Au/CeO_2(cube). The leached counterpart of Au/CeO_2(cube) does not show any activity. To calculate the TOFs the dispersion for the non-leached catalysts was determined from the TEM particle size, while that of Au/CeO_2(rod)-CN was assumed to be one. We expect that the Au/CeO_2(rod) contains also very dispersed gold cations or clusters that were not imaged by EM analysis. As these cations are stable under the oxidizing reaction conditions, the TOF for Au/CeO_2(rod)

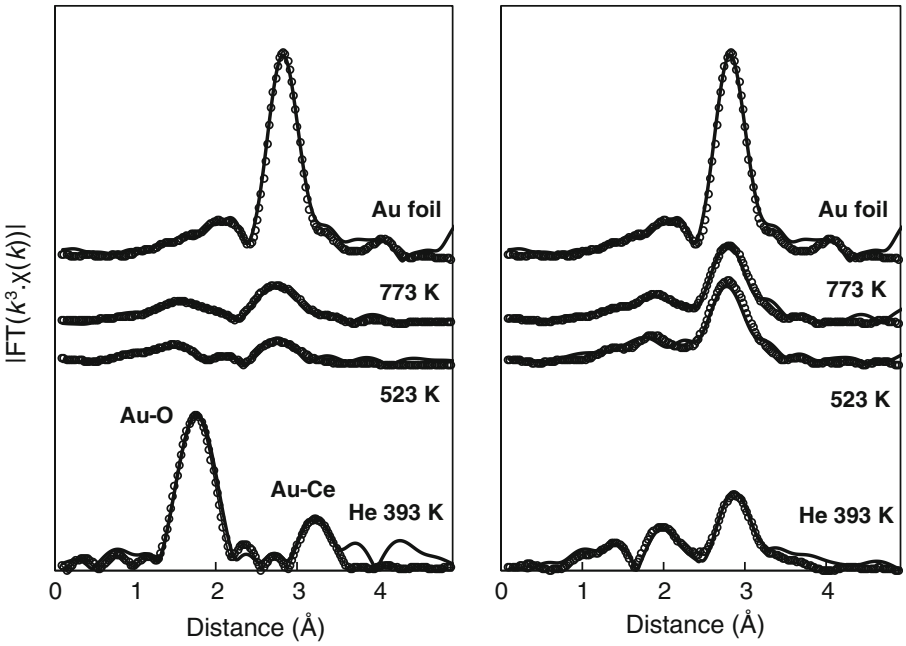

Fig. 8 Experimental (*solid line*) and fitted (*dotted points*) FT EXAFS functions of (*left*) Au/CeO_2(rod)-CN and (*right*) Au/CeO_2(rod) after drying at 393 K and reduction at increasing temperatures. The corresponding spectrum of a Au foil is included

should be a lower bound. Nonetheless, the activity of Au/CeO_2(rod) is substantially higher than that of Au/CeO_2(rod)-CN. Moreover, Au/CeO_2(rod) is much more active than Au/CeO_2(cube), which contains fully reduced gold nanoparticles of the same dispersion. At room temperature, Au/CeO_2(rod) is the only catalyst showing activity in CO oxidation (conversion of 11%).

To understand the importance of the nature of the gold phase in more detail, we compared the CO oxidation activities of the two nanorod-supported gold catalysts after different treatments. CO oxidation was carried out in ramping mode (5 K/min) between room temperature and 373 K. Table 5 compares the CO conversion at 313 K during consecutive runs and after intermittent reduction at various temperatures. The activities of these catalysts increased upon consecutive reaction runs. Reduction at 373 K and higher had a slightly negative effect on the CO conversion of Au/CeO_2(rod) up to 623 K. Reduction of this catalyst at 773 K led to a strong decrease of the activity. Reduction increases the activity of the leached catalyst. Also for this catalyst, a pronounced decrease in CO conversion was noted upon reduction at 773 K. This result is consistent with previous reports that the CO oxidation activity on gold catalyst is very sensitive to the treatments [71, 72]. Clearly, the chemical properties of gold clusters are changing with different pre-treatment conditions.

Figure 9 shows the CO conversion during the WGS reaction as a function of temperature for Au/CeO_2(rod) and Au/CeO_2(rod)-CN. The CO conversion of Au/CeO_2(cube) was below 2% and did not depend on temperature. The catalysts were reduced at 453 K prior to reaction. At 473 K the CO conversion was 2.5% for Au/CeO_2(rod). With temperature the CO conversion increased to about 18% at 673 K. Following the subsequent decrease of the reaction temperature the activities became slightly lower than during the increasing temperature mode. The initial CO

Table 4 Catalytic activities of supports and gold-containing catalysts

Sample	CO oxidation[a] TOF (h^{-1})	Benzylic alcohol oxidation[b] TOF (h^{-1})	Butadiene hydrogenation[c] TOF (s^{-1})
Au/CeO_2(rod)	216	59 (108[d])	0.21
Au/CeO_2(rod)-CN	83	0	0.47
Au/CeO_2(cube)	3	14 (193[d])	0.03
Au/CeO_2(cube)-CN	0	0	0.00

[a] 1 vol% CO and 1 vol% O_2 at 313 K

[b] Liquid phase: 1 mmol benzylic alcohol, 100 mg catalyst, 373 K

[c] 2 vol% 1,3-butadiene in H_2; 383 K

[d] 50 mg catalyst; 40 mg NaOH added

Table 5 CO conversion at 313 K of Au supported on rod-shaped CeO_2 as a function of pretreatment

Sample	CO conversion (%)	
	Au/CeO_2(rod)	Au/CeO_2(rod)-CN
Run 1	44	3
Run 2	46	11
Run 3	51	12
Reduced 373 K	55	18
Reduced 473 K	48	16
Reduced 623 K	41	16
Reduced 773 K	17	5

conversion of Au/CeO_2(rod)-CN at 473 K was about two times higher than that of Au/CeO_2(rod). The CO conversion increased to about 15% at a temperature of 553 K. At this temperature the conversion difference with Au/CeO_2(rod) was a factor two. A further increase of the temperature led to severe deactivation and only after reaction above 633 K a small activity increase was noted. During the decreasing temperature branch the activity of the catalyst was substantially lower than during the increasing temperature branch. To compare the intrinsic activities of these two catalysts, we assume that the dispersion of Au/CeO_2(rod) is that of the fresh catalysts (4.6 nm, $D = 28\%$). Reduction at 523 K of Au/CeO_2(rod)-CN results in a coordination of 4. This implies that (nearly) all gold atoms can participate in the catalysis ($D = 100\%$). A rough approximation learns that Au/CeO_2(rod)-CN is about four times more active per surface gold atom than Au/CeO_2(rod) at a temperature of 533 K. This difference is likely due to the dependence of the oxygen surface coverage as a function of the particle size. Small particles can become more easily oxidized, as is also evident from the above-described CO IR results. Deng et al. [74] have found that gold agglomeration during WGS operation results in loss of surface oxygen and might be an explanation for the loss in activity. The temperature-programmed experiments were repeated with the difference that during the decreasing temperature branch 20 ppm H_2S was added to the reactor feed. This had a detrimental effect on the catalytic activity and no conversion of CO was observed anymore.

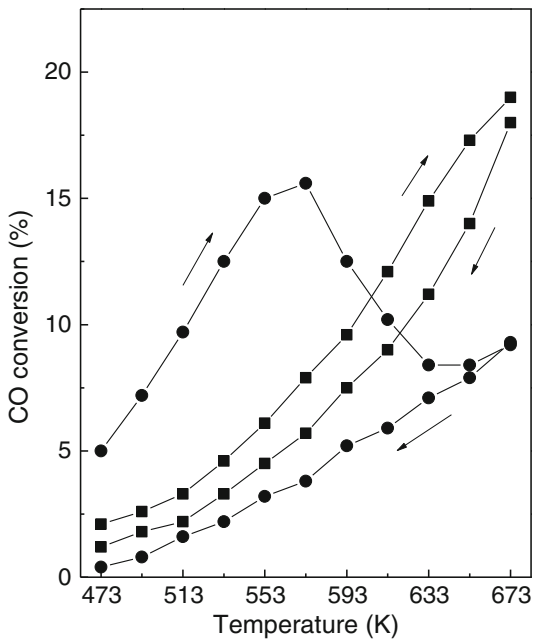

Fig. 9 CO conversion during WGS reaction as a function of temperature of a mixture of 40 vol% N_2, 20 vol% H_2O, 20 vol% H_2, 10 vol% CO and 10 vol% CO_2 of *filled circles* Au/CeO_2(rod) and *filled squares* Au/CeO_2(rod)-CN (*arrows* indicate temperature gradient)

Further experiments concentrated on the role of cationic gold in the WGS reaction. X-ray absorption spectroscopy was employed at 373 and 473 K during the WGS reaction. Flytzani-Stephanopoulos and co-workers [73] already performed such an in situ study and therefore we only briefly discuss these results. Whereas calcined Au/CeO_2(rod)-CN only contained cationic gold (Fig. 6), exposure of this catalyst to an atmosphere of CO/H_2O for 15 min at 373 K resulted in the complete reduction of the gold phase (Fig. 10). The reduction is more extensive than upon treatment in H_2 at 393 K. Treatment in 20% O_2/He led to reoxidation of only 20% of the gold atoms. This shows that the initially isolated gold cations have agglomerated into small Au clusters that can only be partially reoxidized [73]. Under similar conditions Au/CeO_2(rod) contained only metallic gold. EXAFS spectra recorded for Au/CeO_2(rod) after prolonged WGS at 473 K showed a constant Au–Au coordination number of 7.4, which agrees well with the results reported in Table 3. A similar analysis for Au/CeO_2(rod)-CN gave a Au–Au coordination number of 4.4 under WGS conditions. These results show that the gold phases in these materials under WGS conditions are very similar to the gold phases after reduction in H_2. Based on the CO conversion measured during the in situ EXAFS experiments, we again find a higher TOF of 2.2 mol_{CO}/mol_{Au}·min for Au/CeO_2(rod)-CN than the value of 1.3 mol_{CO}/mol_{Au}·min for Au/CeO_2(rod).

Besides gas-phase CO oxidation, gold catalysts have also been reported to be excellent catalyst for selective oxidation of alcohols with molecular oxygen [2, 42, 74]. Table 5 includes the TOFs of the fresh catalysts based on the amount of benzylic alcohol converted and the total amount of gold. The selectivity to benzaldehyde was >99%. The TOF of Au/CeO_2(rod) is substantially higher (59 h^{-1}) than that of Au/CeO_2(cube) at 14 h^{-1}. As the use of base is known to improve the activity in alcohol oxidation of these catalysts, we carried out similar experiments in the presence of a small amount of NaOH. In such case, the activity of Au/CeO_2(rod) and Au/CeO_2(cube) became 108 and 193 h^{-1}, respectively.

Figure 11 shows the activities of the various catalysts in the hydrogenation of 1,3-butadiene at 383 K. The catalysts underwent severe deactivation during the reaction. The butenes selectivity at 383 K remained close to 99% in all cases. The deactivation with time on stream has been reported previously [75] and is likely due to the relatively strong adsorption of butadiene to the catalyst surface. TOFs were calculated based on the butadiene conversion after 3 h time on stream. The TOF of Au/CeO_2(rod) (0.21 s^{-1}) is seven times higher than that of Au/CeO_2(cube) (0.03 s^{-1}) at the same gold loading and particle size. The

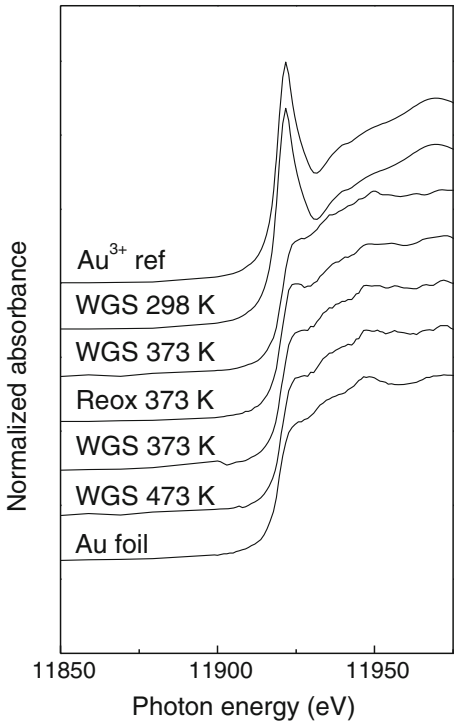

Fig. 10 Near-edge spectra at the Au L_{III} edge of Au/CeO_2(rod)-CN during the WGS reaction and upon reoxidation. Spectra of fresh Au/CeO_2(rod)-CN and a Au foil are shown for reference

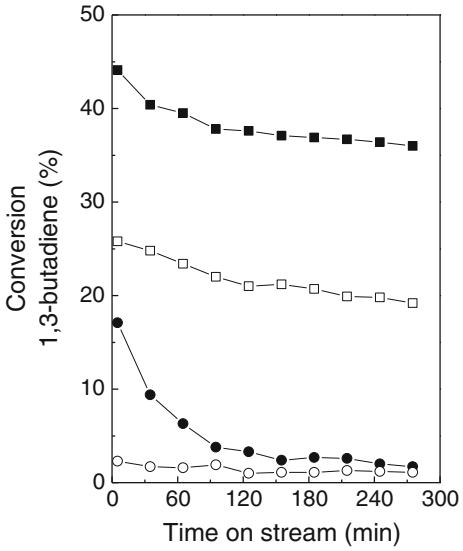

Fig. 11 Butadiene conversion during alkene hydrogenation of *filled squares* Au/CeO_2(rod) and *filled circles* Au/CeO_2(cube) (*open markers* are the cyanide-leached catalysts)

intrinsic activity is even higher after cyanide leaching of Au/CeO_2(rod) and amounts to 0.47 s^{-1}. This difference is consistent with our previous results [11].

4 General Discussion

The results of this study further underpin the notion that the specific surface plane of ceria to which gold atoms binds has a very profound influence on the nature and catalytic activity of gold. These ceria nanorods are most likely enclosed by {110} and {100} surface planes [26, 30, 41]. Deposition–precipitation of gold results in a small fraction of gold atoms that interact so strongly with the ceria surface that these cannot be leached. Calcination results in the dispersion of a more substantial fraction of gold ions into the surface. EXAFS spectroscopy suggests that these Au cations substitute Ce ions in the surface. These dispersed cations resist cyanide leaching. The amount of gold cations that can be accommodated on the nanorods in this manner does not depend on the initial gold loading. This suggests that some specific sites at the ceria nanorod surface are able to accommodate these cations. For a polycrystalline CeO_2 support with a surface area of 80 m^2/g prepared by hydrolysis of $Ce(NO_3)_3$ with urea at 363 K, we found that only 0.08 wt% Au could be retained upon cyanide leaching [11]. The structure around these gold cations is very similar to that determined for Au/CeO_2(rod)-CN. This finding suggests that the higher amount of gold retained in the latter case is due to the higher contribution of {110} surface planes to the surface area of CeO_2(rod) compared to that of CeO_2. Others have suggested that gold cations can form a solid solution with CeO_2 [20, 33, 37–40]. Recently, Kurzman et al. have reported a thermally stable $Au^{3+}O_4$ entity within La_4LiAuO_8 [76].

Characterization shows that reduction of Au/CeO_2(rod)-CN results in very small gold clusters. The FTIR results suggest that these small clusters are present in Au/CeO_2(rod) and Au/CeO_2(rod)-CN. The former catalyst also contains gold nanoparticles. Of importance is that these small gold clusters can be reoxidized to a large extent. In contrast, the gold nanoparticles may accommodate some oxygen atoms at their surface as follows from the changes in the position of the relevant IR band of adsorbed CO. It appears that deposition–precipitation of gold on CeO_2 (cube), which mainly exposes {100} surface planes, only gives reduced gold nanoparticles. The behavior in CO IR spectroscopy upon reduction and oxidation is very similar to that of the nanoparticles in Au/CeO_2(rod). Thus, the main difference between Au/CeO_2(rod) and Au/CeO_2 (cube) is the presence of isolated gold cations stabilized by the {110} in the former. These cations resist cyanide leaching and form finely dispersed gold clusters upon reduction.

The catalytic activity in CO oxidation has been argued to depend on the simultaneous presence of cationic and reduced gold [3]. In accordance with this, Au/CeO_2(cube), which does not contain cationic gold species, has a very

low CO oxidation activity. The Au/CeO_2(rod) catalysts exhibit a higher activity. The intrinsic activity of the leached catalyst is higher than that of the parent one. Fresh Au/CeO_2(rod)-CN is active in CO oxidation at 313 K. Although this may suggest that gold cations are also active for this reaction, Gates and co-workers [63] have shown that very small gold clusters are formed from isolated gold during reaction. The increase of the activity of Au/CeO_2(rod)-CN upon reduction underpins the notion that reduced gold atoms are beneficial for CO oxidation. On the other hand, the high activity appears also to be correlated to the ability of the small gold clusters in Au/CeO_2(rod)-CN to be reoxidized [77]. The observation that part of the high activity of Au/CeO_2(rod) is lost may point to the loss of finely dispersed gold clusters due to agglomeration with the larger nanoparticles. For the case of the leached catalyst, these gold clusters remain dispersed and this provides a reasonable explanation for the higher intrinsic activity in CO oxidation after reduction.

Similarly, clear indications have been found that the presence of surface oxygen at the gold surface is important for high activity in the WGS reaction [73]. Thus, the finely dispersed gold clusters obtained from Au/CeO_2(rod)-CN are more active catalysts than the gold nanoparticles in Au/CeO_2(rod). The higher activity of the leached catalyst is maintained up to reasonably high temperature, whereupon probably more extensive reduction to larger gold nanoparticles occurs [73] and less oxygen can be stabilized. This trend can also be observed from the CO IR data that point to a decreasing contribution of finely dispersed gold with increasing reduction temperature. The WGS reaction conditions appear to be more conducive to gold agglomeration than those involved in CO oxidation and 1,3-butadiene hydrogenation [11], an effect which is undoubtedly due to the presence of water. Moreover, we found that exposure of the gold cations in Au/CeO_2(rod) to the WGS feed (CO/H_2O) at 373 K already results in full reduction in contrast to reduction in H_2 at the same temperature. Au/CeO_2(cube) does not contain cationic gold and accordingly shows a very low activity in the WGS reaction [26].

The catalytic activity of these catalysts in the selective oxidation of benzylic alcohol is related to the presence of metallic gold particles. The gold cations in Au/CeO_2(rod)-CN do not show any activity. It has been put forward that C–H bond cleavage at the gold surface is the rate limiting step in alcohol oxidation [78, 79]. Another important step is the proton abstraction from the alcohol group. Indeed, very often a soluble base is added to facilitate this reaction [80]. The support may also act as a base [42]. In the absence of a base, O–H bond activation may be slow and, in such case, surface oxygen atoms may facilitate this process. Interestingly, the activity of Au/CeO_2(rod) is higher than that of Au/CeO_2(cube) in the absence of a soluble base. A tentative explanation is the role of the CeO_2 surface or of the gold cations in oxygen activation, thus facilitating alcohol activation. Indeed, both catalysts become much more active upon addition of NaOH. Thus, without base the O–H bond cleavage is argued to be the rate limiting step, while this shifts to C–H bond activation in the presence of NaOH. In the latter case, the gold nanoparticles on the surface of ceria nanocubes are much more active than those on the surface of nanorod ceria. The reason for the substantially higher activity of Au/CeO_2(cube) remains unclear here.

The intrinsic activity in 1,3-butadiene hydrogenation of Au/CeO_2(rod)-CN (TOF = 0.47 s^{-1}) is higher than that of its unleached counterpart (TOF = 0.21 s^{-1}). These results are in qualitative agreement with the results for a gold catalyst supported by polycrystalline CeO_2 [11]. The activity difference is however substantially smaller and this is related to the relatively low reduction temperature of 393 K employed in this study. As follows from the near-edge spectra, a substantial part of the gold phase in Au/CeO_2(rod)-CN remains in the oxidic phase. The catalysts deactivate slightly with reaction time, which is due to some coke formation on the surface as is evident from the color change of the catalysts.

5 Conclusions

The gold phase supported on ceria nanorods and nanocubes shows a strong dependence of the catalytic activity on the exposed surface planes of ceria. After standard deposition–precipitation, both forms of ceria contain gold nanoparticles in the range 2–6 nm, which can be removed by cyanide leaching. Additionally, the ceria nanorods stabilize a small amount of gold cations, which resist cyanide leaching. EXAFS of the leached ceria nanorod catalyst shows that the gold cations replace Ce ions in the surface plane of the nanorods. Upon reduction these isolated Au atoms form finely dispersed Au clusters with a high activity in CO oxidation, the WGS reaction and 1,3-butadiene hydrogenation. By analogy with the very low activity of reduced gold nanoparticles on ceria nanocubes exposing the {100} surface plane, it is inferred that the gold nanoparticles on the ceria nanorod surface also have a low activity in such reactions. For liquid phase alcohol oxidation, metallic gold nanoparticles are the active sites. In the absence of a base, the O–H bond cleavage appears to be rate limiting, while this shifts to C–H bond activation after addition of NaOH. In the latter case, the gold nanoparticles on the surface of ceria nanocubes are much more active than those on the surface of nanorod ceria.

Acknowledgments This work was financially supported by the National Research School Combination Catalysis (NRSC-Catalysis) and the Program for Strategic Scientific Alliances between China and Netherlands funded by the Royal Netherlands Academy of Arts and Science and the Chinese Ministry of Science and Technology. We thank the Soft Matter Cryo-TEM Research Unit for access to the TEM facility, NWO for access to X-ray absorption spectroscopy facilities at ESRF and ESRF staff for their support.

References

1. Bond GC, Louis C, Thompson DT (2007) Catalysis by gold. Imperial College Press, London
2. Corma A, Garcia H (2008) Chem Soc Rev 37:2096
3. Fierro-Gonzalez JC, Gates BC (2008) Chem Soc Rev 37:2127
4. Haruta M, Yamada N, Kobayashi T, Iijima S (1989) J Catal 115:301
5. Esch F, Fabris S, Zhou L, Montini T, Africh C, Fornasiero P, Comelli G, Rosei R (2005) Science 309:752
6. Campbell C, Peden C (2005) Science 309:713
7. Fierro-Gonzales JC, Gates BC (2004) J Phys Chem B 108:16999
8. Fierro-Gonzales JC, Gates BC (2007) Catal Today 122:201
9. Enache DI, Knight DW, Hutchings GJ (2005) Catal Lett 103:43
10. Azizi Y, Petit C, Pitchon V (2008) J Catal 256:338
11. Guan Y, Hensen EJM (2009) Phys Chem Chem Phys 11:9578
12. Fu Q, Saltsburg H, Flytzani-Stephanopoulos M (2003) Science 301:935
13. Kim CH, Thompson LT (2006) J Catal 244:248
14. Karpenko A, Leppelt R, Plzak V, Behm RJ (2007) J Catal 252:231
15. Claus P, Brückner A, Mohr C, Hofmeister H (2000) J Am Chem Soc 122:11430
16. Guzman J, Gates BC (2003) Angew Chem Int Ed 42:690
17. Zhang X, Shi H, Xu BQ (2005) Angew Chem Int Ed 44:7132
18. Fu Q, Weber A, Flytzani-Stephanopoulos M (2001) Catal Lett 77:87
19. Carrettin S, Concepcion P, Corma A, Nieto JML, Puntes VF (2004) Angew Chem Int Ed 43:2538
20. Venezia AM, Pantaleo G, Longo A, Carlo GD, Casaletto MP, Liotta FL, Deganello G (2005) J Phys Chem B 109:2821
21. Abad A, Concepcion P, Corma A, Garcia H (2005) Angew Chem Int Ed 44:4066
22. Lai SY, Qiu YF, Wang SJ (2006) J Catal 237:303
23. Tang Z, Edwards JK, Bartley JK, Taylor SH, Carley AF, Herzing AA, Kiely CJ, Hutchings GJ (2007) J Catal 249:218
24. Yuan ZY, Idakiev V, Vantomme A, Tabakova T, Ren TZ, Su BL (2008) Catal Today 131:203
25. Jia KM, Zhang HL, Li WC (2008) Chin J Catal 29:1089
26. Si R, Flytzani-Stephanopoulos M (2008) Angew Chem Int Ed 47:2884
27. Huang XS, Sun H, Wang LC, Liu YM, Fan KN, Cao Y (2009) Appl Catal B 90:224
28. Yi GQ, Xu ZN, Guo GC, Tanaka K, Yuan YZ (2009) Chem Phys Lett 479:128
29. Zhang YW, Si R, Liao CS, Yan CH, Xiao CX, Kou Y (2003) J Phys Chem B 107:10159
30. Mai HX, Sun LD, Zhang YW, Si R, Feng W, Zhang HP, Liu HC, Yan CH (2005) J Phys Chem B 109:24380
31. Lu JL, Gao HJ, Shaikhutdinov S, Freund HJ (2007) Catal Lett 114:8
32. Tibiletti D, Amieiro-Fonseca A, Burch R, Chen Y, Fisher J, Goguet A, Hardacre C, Hu P, Thompsett A (2005) J Phys Chem B 109:22553
33. Zhang CJ, Michaelides A, King DA, Jenkins SJ (2009) J Phys Chem C 113:6411
34. Baron M, Bondarchuk O, Stacchiola D, Shaikhutdinov S, Freund HJ (2009) J Phys Chem C 113:6042
35. Castellani NJ, Branda MA, Neyman KM, Illas F (2009) J Phys Chem C 113:4948
36. Chen Y, Hu P, Lee MH, Wang HF (2008) Surf Sci 602:1736
37. Camellone MF, Fabris S (2009) J Am Chem Soc 131:10473
38. Shapovalov V, Metiu H (2007) J Catal 245:205
39. Skoda M, Cabala M, Matolinova I, Prince KC, Skala T, Sutara F, Veltruska K, Matolin V (2009) J Chem Phys 130:034703
40. Zhang CJ, Michaelides A, King DA, Jenkins SJ (2008) J Chem Phys 129:194708
41. Zhou KB, Wang X, Sun XM, Peng Q, Li YD (2005) J Catal 229:206
42. Yang J, Guan YJ, Verhoeven T, van Santen R, Li C, Hensen EJM (2009) Green Chem 11:322
43. Liu XW, Zhou KB, Wang L, Wang BY, Li YD (2009) J Am Chem Soc 131:3140
44. Akita T, Okumura M, Tanaka K, Kohyama M, Haruta M (2005) J Mater Sci 40:3101
45. Akita T, Tanaka K, Kohyama M (2008) J Mater Sci 43:3917
46. Majimel J, Lamirand-Majimel M, Moog I, Feral-Martin C, Treguer-Delapierre M (2009) J Phys Chem C 113:9275
47. Perrichon V, Laachir A, Bergeret G, Frety R, Tournayan L, Touret O (1994) J Chem Soc Faraday Trans 90:773
48. Fu Q, Deng WL, Saltsburg H, Flytzani-Stephanopoulos M (2005) Appl Catal B Environ 56:57
49. Delannoy L, Weiher N, Tsapatsaris N, Beesley AM, Nchari L, Schroeder SLM, Louis C (2007) Top Catal 44:263
50. Corma A, Boronat M, Gonzalez S, Illas F (2007) Chem Commun 3371
51. Fujitani T, Nakamura I, Akita T, Okumura M, Haruta M (2009) Angew Chem Int Ed 48:9515
52. Kartusch C, van Bokhoven JA (2009) Gold Bull 42:343
53. Guzman J, Carrettin S, Corma A (2005) J Am Chem Soc 127:3286
54. Laachir A, Perrichon V, Badri A, Lamotte J, Catherine E, Lavalley JC, Elfallah J, Hilaire L, Lenormand F, Quemere E, Sauvion GN, Touret O (1991) J Chem Soc Faraday Trans 87:1601
55. Daly H, Ni J, Thompsett D, Meunier FC (2008) J Catal 254:238
56. Mihaylov M, Knozinger H, Hadjiivanov K, Gates BC (2007) Chem Ing Tech 79:795
57. Menegazzo F, Manzoli M, Chiorino A, Boccuzzi F, Tabakova T, Signoretto M, Pinna F, Pernicone N (2006) J Catal 237:431
58. Chiorino A, Manzoli M, Menegazzo F, Signoretto M, Vindigni F, Pinna F, Boccuzzi F (2009) J Catal 262:169
59. Vindigni F, Manzoli M, Chiorino A, Boccuzzi F (2009) Gold Bull 42:106
60. Guan Y, Hensen EJM (2009) Appl Catal A Gen 361:49
61. Aguilar-Guerrero V, Gates BC (2007) Chem Commun 3210
62. Fierro-Gonzalez JC, Guzman J, Gates BC (2007) Top Catal 44:103
63. Aguilar-Guerrero V, Gates BC (2008) J Catal 260:351
64. Hao YL, Gates BC (2009) J Catal 263:83
65. Aguilar-Guerrero V, Lobo-Lapidus RJ, Gates BC (2009) J Phys Chem C 113:3259
66. Miller JT, Kropf AJ, Zha Y, Regalbuto JR, Delannoy L, Louis C, Bus E, van Bokhoven JA (2006) J Catal 240:222
67. Jones PG, Rumpel H, Schwarzmann E, Sheldrick GM (1979) Acta Crystallogr Sect B Struct Crystallogr Cryst Chem 35:1435

68. Wang J, Wang G, Zhao J (2002) Phys Rev B Condens Matter 66:35418
69. Soule de Bas B, Ford MJ, Cortie MB (2004) J Mol Struct (THEOCHEM) 686:193
70. Jain PK (2005) Struct Chem 16:421
71. Simakov A, Tuzovskaya I, Pestryakov A, Bogdanchikov N, Gurin V, Avalos M, Farias MH (2007) Appl Catal A Gen 331:121
72. Wang XY, Wang SP, Wang SR, Zhao YQ, Huang J, Zhang SM, Huang WP, Wu SH (2006) Catal Lett 112:115
73. Deng W, Frenkel AI, Si R, Flytzani-Stephanopoulos M (2008) J Phys Chem C 112:12834
74. Della Pina C, Falletta E, Prati L, Rossi M (2008) Chem Soc Rev 37:2077
75. Schimpf S, Lucas M, Mohr C, Rodemerck U, Bruckner A, Radnik J, Hofmeister H, Claus P (2002) Catal Today 72:265
76. Kurzman JA, Ouyang XY, Im WB, Li J, Hu J, Scott SL, Seshadri R (2010) Inorg Chem 49:4670
77. Bond GC (2010) Gold Bull 43:88
78. Abad A, Corma A, Garcia H (2008) Chem Eur J 14:212
79. Conte M, Miyamura H, Kobayashi S, Chechik V (2009) J Am Chem Soc 131:7189
80. Hutchings GJ, Carrettin S, Landon P, Edwards JK, Enache D, Knight DW, Xu YJ, Carley AF (2006) Top Catal 38:223